

# Three-Dimensional Modeling of a Fin-Actuated Robotic Fish with Multimodal Swimming

Wei Wang<sup>1,2</sup>, Xia Dai<sup>3</sup>, Liang Li<sup>1</sup>, Banti Gheneti<sup>2</sup>, Yang Ding<sup>4</sup>, Junzhi Yu<sup>5</sup>, and Guangming Xie<sup>1,6</sup>

**Abstract**—Dynamical model is always an important factor in controller design for robots. Existing models of robotic fish typically incorporate only planar motion, rarely considering spatial motion. This paper formulates a complete 3D dynamic model for the robotic fish actuated by pectoral and caudal fins, in which the fluid forces mainly contain quasi-steady lift and drag, gravity and buoyancy, and waterjet strike force. The critical lift and drag of flapping fins are derived with an explicit 3D angle of attack. Taking a bio-inspired central pattern generator (CPG) as the system actuation, our model can produce multimodal maneuvers, including forward/backward swimming, turning, and ascending/descending, as well as complicated motions such as rolling and spiraling. Motions simulated in a 3D environment are experimentally validated with a free-swimming robotic fish. Furthermore, systematic comparisons between simulations and experiments are conducted over a wide range of the control parameter space for beating frequency, amplitude and offset. The overall results demonstrate the effectiveness and the versatility of the developed 3D dynamic model in the prediction of the robot trajectory, velocity, and attitude.

**Index Terms**—Three-dimensional modeling, biologically inspired robots, robot dynamics, marine robotics, robotic fish.

## I. INTRODUCTION

THE maneuverability, efficiency and motion stability of fish substantially exceed those of current underwater vehicles. These outstanding characteristics make fish an excellent source of inspiration for scientists and engineers aiming to design and build versatile underwater vehicles. As a consequence, there has been an ever-growing interest in developing biologically inspired robotic fish over the past two decades [1], [2], such as lifelike 3D swimming robotic fish [3], [4], amphibious robotic fish [5], boxfish-like robots [6]–[8], robotic manta ray [9], robotic mackerel [10], two-caudal-fin

robotic fish [11], wire-driven robotic fish [12], and soft robotic fish [13]. Robotic fish have great potential for many marine applications, including underwater exploration, mobile sensing and environmental monitoring [14]–[16]. In addition, robotic fish can also serve as a controllable high-fidelity platform to study multi-robot control [17], [18].

As a fundamental issue for designing robotic fish, the modeling of fish dynamics has attracted a lot of attention [19]–[23]. Lighthill's elongated body theory [24] and large-amplitude elongated body theory [25] are widely accepted methods for modeling robotic fish [22], [26]–[29] because of their good balance between fidelity and simplicity. Quasi-steady hydrofoil theory has also been extensively adopted to model fish robot dynamics since it has been demonstrated to be effective, flexible and tractable [19]–[21], [30]–[32]. Additionally, by solving the Navier-Stokes equation, a faithful hydrodynamic force distribution can be computed through computational fluid dynamics (CFD) simulation [33], [34]. More recently, by using the linear Euler-Bernoulli beam model, several groups have attempted to model the flexible body and fins of natural fish [35], [36]. These fish dynamics studies have progressively advanced the understanding of fish swimming and the controller design of robotic fish.

At present, the vast majority of existing studies of fish robot modeling have focused on planar motions. Notice that fish always rely on multiple fins to achieve efficient 3D movements such as pitching and rolling maneuvers. Hence, 3D modeling of robotic fish will facilitate the understanding of 3D motions in fish swimming and the design of 3D motion controllers of robotic fish. Several groups [20], [21], [26] have preliminarily studied the 3D modeling of robotic fish in the literature. For instance, Boyer *et al.* [20] simulated 3D locomotion of an eel-like robot by using a continuum model which considers elemental quasi-static lift and drag. Morgansen *et al.* [21] developed 3D equations of motion for their robotic fish and briefly verified the model through forward motion, turning motion, and depth control. However, these 3D models are typically incomplete in predicting multimodal 3D behaviors, especially complicated 3D movements such as rolling and spiraling. In addition, these studies either involve only simulation (e.g., [20]) or contain limited experimental validation (e.g., [21], [26]). Lastly, the versatility of these 3D dynamic models was not validated over large scopes of the parameter space.

This paper addresses the above problems in the previous 3D modeling of robotic fish, and contributes in the following three aspects: 1) the formulation of a complete 3D dynamic model capable of producing multimodal motions of robotic fish including forward and backward swimming, turning, pitching

This work was supported in part by grants from the National Natural Science Foundation of China (NSFC, No. 51575005, 61503008, 61633002, 91648120) and the China Postdoctoral Science Foundation (No. 2015M570013, 2016T90016).

<sup>1</sup> W. Wang, L. Li, and G. Xie are with the State Key Laboratory for Turbulence and Complex Systems, College of Engineering, Peking University, Beijing 100871, China. (email: {wangweiw4y4, liatli, xiegming}@pku.edu.cn).

<sup>2</sup> W. Wang and B. Gheneti are with the Department of Urban Studies and Planning, Massachusetts Institute of Technology, Cambridge, MA 02139, USA. (email: {wwewang, bgheneti}@mit.edu).

<sup>3</sup> X. Dai is with the School of Electronics and Information Engineering, Beihang University, Beijing 100191, China. (e-mail: sunnydora01@hotmail.com).

<sup>4</sup> Y. Ding is with the Beijing Computational Science Research Center, No. 10 Dongbeiwang West Road, Hai-Dian District, Beijing 100094, China. (email: dingyang@csrc.ac.cn).

<sup>5</sup> J. Yu is with the State Key Laboratory of Management and Control for Complex Systems, Institute of Automation, Chinese Academy of Sciences, Beijing 100190, China (e-mail: junzhi.yu@ia.ac.cn).

<sup>6</sup> G. Xie are with the Institute of Ocean Research, Peking University, Beijing, 100871, China. (email: xiegming@pku.edu.cn).

and complicated motions such as rolling and spiraling; 2) the experimental validation of the developed 3D model for these multimodal motions; 3) the versatility validation of the 3D model within large scopes of parameter space through systematic comparisons between the simulated and experimental data. A more detailed account of the contributions follow.

In this paper, we adopt quasi-steady hydrofoil theory as the main framework because it benefits the construction of 3D motions and effectively balances fidelity and simplicity [20], [21]. Critically, the angle of attack of the flapping fins are derived in an exact 3D form. Furthermore, the 3D lift and drag of the flapping fins are explicitly expressed with the angle of attack for the first time, which largely guarantees the generation of multimodal 3D motions. Note that Lighthill's elongated-body theory is restricted to planar motions, although it strikes a sound balance between fidelity and simplicity [37]. One can also consider the CFD method to obtain a faithful robot model. However, this computationally expensive approach is not amenable to designing a controller for the robot. Systematic comparisons between the simulations and experiments show that the formulated model is able to predict the robot's key features such as the velocity, attitude and the body oscillation within a wide range of control parameters. We admit that the developed 3D model cannot capture every detail of the fluid-body interactions. However, the Newton-Euler forms of the 3D dynamic model will facilitate the design of 3D motion controllers for fin-actuated underwater robots. Indeed, capturing all fluid flow details is not always necessary for robot control, because control feedback can often compensate for reasonable modeling errors.

The remainder of this paper is organized as follows. Section II describes the prototype of the robotic fish. The 3D dynamic model for robotic fish is formulated in Section III. Simulations and experimental results for multiple 3D motions are systematically analyzed in Section IV. Conclusions and future work are given at the end of this paper.

## II. ROBOT PROTOTYPE OVERVIEW

The robot prototype is inspired by ostraciiform swimmers which always have a rigid body and rely on their multiple fins to propel and maneuver. As shown in Fig. 1, the prototype consists of a well-streamlined rigid body, a pair of rigid pectoral fins and a rigid caudal fin. The mass distribution of the robot is carefully designed to facilitate 3D motions. First, the center of mass (C. M.) of the robot is calculated by setting the density/mass of each component in Solidworks. Second, the center of buoyancy (C. B.) of the robot can be acquired through Solidworks by assuming the robot has a uniform mass distribution. Finally, the robot density is designed close to  $1000 \text{ kg/m}^3$ . The C. M. of the robot is slightly lower than but on the same vertical axis as the C. B.. These features facilitate both the planar and 3D motions of the robot.

The main controller of the robot adopts a credit-card sized computer, Raspberry Pi 2. It is responsible for high-level tasks, such as image processing, localization, and motion planning. Moreover, three STM32 microcontrollers acting as auxiliary processors are used for locomotion control, attitude calculation

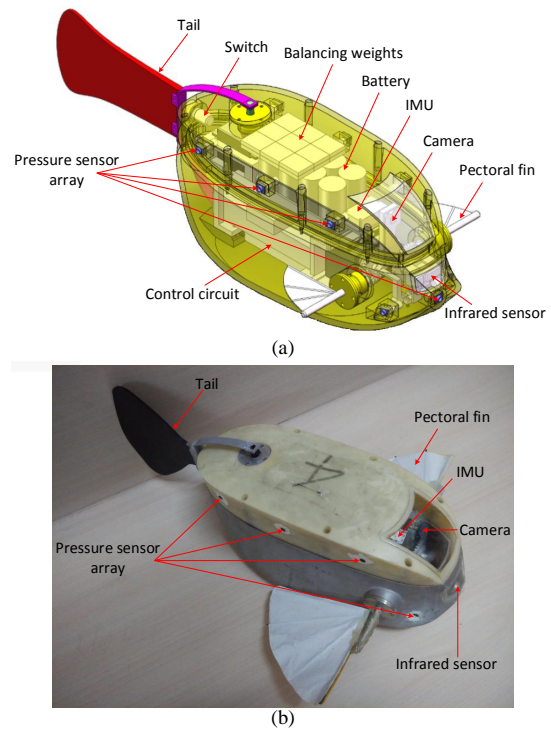


Fig. 1. Mechanical and hardware configurations of the fish robot. (a) Concept design; (b) robot prototype.

and data acquisition. Fig. 2 shows the implementation diagram of the robot control system. Moreover, the robot integrates

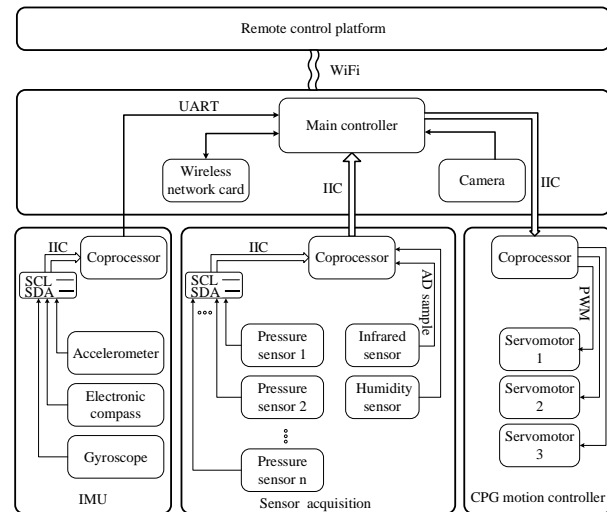


Fig. 2. Implementation diagram for the robot control system. The arrays indicate the information flow.

several types of sensors onboard. An inertial measurement unit (IMU) is fixed parallel to the body principal axes to monitor the robot pitch, yaw and roll angles, angular velocity and acceleration. Pressure sensors are distributed on the surface of robot. The camera and infrared sensor are not used in this study. The robot is operated by a Linux system (Debian), and the specifications are listed in Table I.

The locomotion of the robot is controlled by a central pattern generator (CPG) network [38], [39] defined as follows

TABLE I  
TECHNICAL SPECIFICATIONS OF THE ROBOT PROTOTYPE

Items	Characteristics
Dimension(L × W × H)	~ 400 mm × 140 mm × 142 mm
Total mass	~ 3.1 kg
Drive mode	DC servomotors (12.9 kg-cm)
Onboard sensors	Camera, IMU, pressure sensor, and infrared sensor
Power supply	9.6 V rechargeable Ni-MH batteries
Operation time	~ 5 h
Control mode	Autonomous/Wireless mode

$$\dot{p}_i = \kappa_i(P_i - p_i) \quad (1a)$$

$$\dot{o}_i = v_i(O_i - o_i) \quad (1b)$$

$$\dot{\tau}_i = 2\pi f_i + \sum_{j \in T_i} \mu_{ij}(\tau_j - \tau_i - \phi_{ij}) \quad (1c)$$

$$\zeta_i = o_i + p_i \sin(\tau_i) \quad (1d)$$

where  $p_i$ ,  $o_i$ , and  $\tau_i$  are state variables representing the amplitude, offset and phase of the  $i^{\text{th}}$  oscillator, and  $\zeta_i$  is the output of the CPG controller.  $f_i$ ,  $P_i$  and  $O_i$  are control parameters for the desired frequency, amplitude and offset of the  $i^{\text{th}}$  oscillator.  $\mu_{ij}$  and  $\phi_{ij}$  determine the coupling weight and phase bias between the  $j^{\text{th}}$  oscillator and  $i^{\text{th}}$  oscillator respectively.  $\kappa_i$  and  $v_i$  are constants representing the convergence speed of the  $i^{\text{th}}$  oscillator.  $T_i$  is the set of neighbors of the  $i^{\text{th}}$  oscillator. Subscripts  $i = 1, 2, 3$  represent the left pectoral fin, right pectoral fin and caudal fin of the robot respectively. The CPG controller is implemented on the SMT32 microcontroller/coprocessor shown in Fig. 2. Discretization is required for implementing our continuous CPG model on a digital microcontroller. The eulerian difference method is applied to balance the limited computing power of microcontrollers and calculation precision. More implementation details of the CPG controller can be found in our previous work [40].

In this study, CPG serves as the actuation of the robot system to generate multiple 3D motions such as forward and backward swimming, turning, ascending and descending, both in simulations and experiments. For simplicity, the frequencies of the robot oscillators are the same ( $f_i = f$ ), and the phase biases  $\phi_{ij}$  equal zero. The CPG parameters become  $\{f, P_i, O_i\}$  in this study.

### III. 3D DYNAMIC MODEL

Fig. 3 shows a diagram of the system, consisting of a rigid robotic fish body, a pair of active rigid pectoral fins and an active rigid tail. We use  $[\mathbf{X}, \mathbf{Y}, \mathbf{Z}]$  to denote inertial coordinates,  $[\mathbf{x}, \mathbf{y}, \mathbf{z}]$  to denote body-fixed coordinates with unit vectors  $[\hat{\mathbf{x}}, \hat{\mathbf{y}}, \hat{\mathbf{z}}]$ , and  $[\mathbf{x}_i, \mathbf{y}_i, \mathbf{z}_i]$  to denote three fin-fixed coordinates. Origins of  $[\mathbf{x}_1, \mathbf{y}_1, \mathbf{z}_1]$ ,  $[\mathbf{x}_2, \mathbf{y}_2, \mathbf{z}_2]$  and  $[\mathbf{x}_3, \mathbf{y}_3, \mathbf{z}_3]$  are expressed as  $(a_l, -b_l, c_l)$ ,  $(a_r, b_r, c_r)$  and  $(-a_t, b_t, c_t)$  in the body-fixed coordinates, respectively. The velocity of the robot is denoted by  $\mathbf{V}$  with unit vector  $\hat{\mathbf{V}}$ , consisting of longitudinal velocity  $V_x$ , lateral velocity  $V_y$  and vertical velocity  $V_z$ , expressed in the body-fixed coordinates. The roll, pitch and yaw of the robot are respectively denoted by  $\phi$ ,  $\theta$  and  $\psi$ , and the angular velocity is denoted by  $\boldsymbol{\omega} = [\omega_x \ \omega_y \ \omega_z]^T$ .

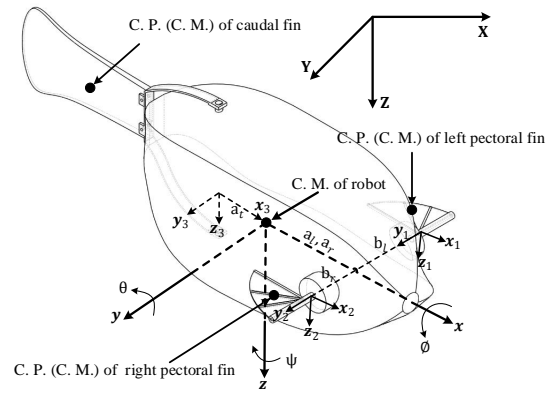


Fig. 3. Oblique view of the robot undergoing 3D motions.

#### A. Kinematic Analysis

The total force on the fin is supposed to act on its center of pressure (C. P.). We assume C. P. is coincident with the C. M. of the fin in this study. The fin velocity expressed in the body-fixed coordinates is denoted by

$$\mathbf{v}_i = \mathbf{V} + \boldsymbol{\omega} \times \mathbf{I}_i + \mathbf{v}_r^i \quad (2)$$

where  $\mathbf{I}_i$  denotes the vector from the body center to the C. P. of the  $i^{\text{th}}$  fin,  $\mathbf{v}_r^i$  is the velocity of the  $i^{\text{th}}$  fin relative to the robot body, and “ $\times$ ” represents the cross product of vectors. Similarly,  $\hat{\mathbf{v}}_i$  is the unit vector of  $\mathbf{v}_i$ . According to the robot configurations in Fig. 3,  $\mathbf{I}_i$  is expressed as

$$\begin{cases} \mathbf{I}_1 = (a_l - r_x \cos \zeta_1) \hat{\mathbf{x}} - (b_l + r_y) \hat{\mathbf{y}} + (c_l + r_x \sin \zeta_1) \hat{\mathbf{z}} \\ \mathbf{I}_2 = (a_r - r_x \cos \zeta_2) \hat{\mathbf{x}} + (b_r + r_y) \hat{\mathbf{y}} + (c_r + r_x \sin \zeta_2) \hat{\mathbf{z}} \\ \mathbf{I}_3 = -(a_c + r_c \cos \zeta_3) \hat{\mathbf{x}} + r_c \sin \zeta_3 \hat{\mathbf{y}} + c_c \hat{\mathbf{z}} \end{cases} \quad (3)$$

where  $r_c$  denotes the distance between C. P. of the caudal fin and the origin of the caudal fin fixed coordinates. We define the distance between C. P. of the left (right) pectoral fin and the origin of the left (right) pectoral fin fixed coordinates as  $(r_x^2 + r_y^2)^{1/2}$  where  $r_x$  and  $r_y$  are the distance components along the  $\mathbf{x}_1/\mathbf{x}_2$  axis and along the  $\mathbf{y}_1/\mathbf{y}_2$  axis, respectively. We can derive  $\mathbf{v}_r^i$  in (2) from the robot configurations

$$\begin{cases} \mathbf{v}_r^1 = r_x \dot{\zeta}_1 \sin \zeta_1 \hat{\mathbf{x}} - r_x \dot{\zeta}_1 \cos \zeta_1 \hat{\mathbf{z}} \\ \mathbf{v}_r^2 = r_x \dot{\zeta}_2 \sin \zeta_2 \hat{\mathbf{x}} - r_x \dot{\zeta}_2 \cos \zeta_2 \hat{\mathbf{z}} \\ \mathbf{v}_r^3 = r_c \dot{\zeta}_3 \sin \zeta_3 \hat{\mathbf{x}} + r_c \dot{\zeta}_3 \cos \zeta_3 \hat{\mathbf{y}} \end{cases} \quad (4)$$

#### B. Evaluation of Hydrodynamic Forces

We mainly consider four types of hydrodynamic forces for the robot: the lift and drag caused by the fin motions, the lift and drag caused by the body, the gravity and buoyancy acting on the body and the water strike forces.

We first analyze the lift and drag caused by the fin motions. Lift is defined as the force acting perpendicular to the direction of the motion and drag as that acting parallel to the direction of the motion, as shown in Fig. 4. Because the robotic fins always move at a high Reynolds number, the lift  $F_L^i$  and drag  $F_D^i$  of the  $i^{\text{th}}$  fin can be described as follows [41], [42]

$$F_L^i = \frac{1}{2} \rho (c_{L1}^i \alpha_i + c_{L2}^i \alpha_i^2 + o(\alpha_i^2)) |\mathbf{v}_i|^2 S_i \quad (5)$$

$$F_D^i = \frac{1}{2} \rho (c_{D0}^i + c_{D1}^i \alpha_i + c_{D2}^i \alpha_i^2 + o(\alpha_i^2)) |\mathbf{v}_i|^2 S_i \quad (6)$$

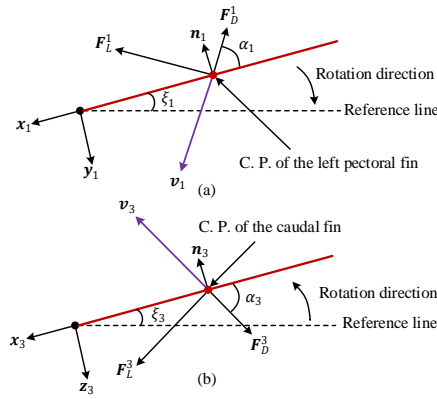


Fig. 4. Lift and drag acting on the moving fins. (a) Side view for left pectoral fin; (b) Top view for tail. Red lines stand for the moving fins.  $\mathbf{n}_1$  and  $\mathbf{n}_3$  denote the normal vectors of left pectoral fin and tail surfaces, respectively.

where  $\rho$  is the density of water,  $\alpha_i$  is the angle of attack for the  $i^{\text{th}}$  fin denoting the angle between the reference line of the robot's fin and the oncoming flow,  $S_i$  is the surface area for the  $i^{\text{th}}$  fin,  $c_{D0}^i$ ,  $c_{D1}^i$  and  $c_{D2}^i$  are the drag coefficients for the  $i^{\text{th}}$  fin,  $c_{L1}^i$  and  $c_{L2}^i$  are the lift coefficients for the  $i^{\text{th}}$  fin, and  $o(\alpha_i^2)$  is the second-order infinitesimal of  $\alpha_i$ . In particular, the expressions of lift and drag coefficients are derived from [41], where the lift and drag coefficients are formulated as trigonometric functions of angle of attack. Similarly, in this paper we use polynomial functions to approximate these trigonometric relations between lift/drag coefficients and the angle of attack. Moreover, the drag acting on the robotic fin is expressed in the body-fixed coordinates as

$$\mathbf{F}_D^i = -F_D^i \hat{\mathbf{v}}_i \quad (7)$$

The normal vector of the  $i^{\text{th}}$  fin surface is expressed as follows in the body-fixed coordinates

$$\begin{cases} \mathbf{n}_1 = \sin \zeta_1 \hat{\mathbf{x}} - \cos \zeta_1 \hat{\mathbf{z}} \\ \mathbf{n}_2 = \sin \zeta_2 \hat{\mathbf{x}} - \cos \zeta_2 \hat{\mathbf{z}} \\ \mathbf{n}_3 = \sin \zeta_3 \hat{\mathbf{x}} + \cos \zeta_3 \hat{\mathbf{y}} \end{cases} \quad (8)$$

The lift acting on the robotic fins is expressed in the body-fixed coordinates as

$$\mathbf{F}_L^i = \begin{cases} \frac{\hat{\mathbf{v}}_i \sin \alpha_i - \mathbf{n}_i}{|\hat{\mathbf{v}}_i \sin \alpha_i - \mathbf{n}_i|} F_L^i, & \text{if } \mathbf{n}_i \cdot \hat{\mathbf{v}}_i > 0 \\ \frac{\hat{\mathbf{v}}_i \sin \alpha_i + \mathbf{n}_i}{|\hat{\mathbf{v}}_i \sin \alpha_i + \mathbf{n}_i|} F_L^i, & \text{if } \mathbf{n}_i \cdot \hat{\mathbf{v}}_i \leq 0 \end{cases} \quad (9)$$

where the angle of attack  $\alpha_i$  is explicitly defined for the first time in 3D space

$$\alpha_i = |\arcsin(\mathbf{n}_i \cdot \hat{\mathbf{v}}_i)| \quad (10)$$

Since the robot dynamics are calculated in the body-fixed coordinates, the drag and lift acting on the fins will form torques with respect to the C. M. of the robot body

$$\mathbf{M}_i = \mathbf{I}_i \times (\mathbf{F}_D^i + \mathbf{F}_L^i) \quad (11)$$

where  $\mathbf{M}_i$  is the sum of drag and lift moments acting on the C. M. of the robot body caused by the  $i^{\text{th}}$  fin motion.

Now we calculate the gravitational force and buoyancy acting on the robot. The gravitational acceleration vector

is expressed as  $R^T \mathbf{g}$  in the body-fixed coordinates, where  $\mathbf{g} = [0, 0, g]^T$  ( $g = 9.8 \text{ m/s}^2$ ) and  $R$  is the transform matrix from body-fixed frame to earth-fixed frame

$$R = \begin{bmatrix} c_\theta c_\psi & s_\phi s_\theta c_\psi - c_\phi s_\psi & c_\phi s_\theta c_\psi + s_\phi s_\psi \\ c_\theta s_\psi & s_\phi s_\theta s_\psi + c_\phi c_\psi & c_\phi s_\theta s_\psi - s_\phi c_\psi \\ -s_\theta & s_\phi c_\theta & c_\phi c_\theta \end{bmatrix} \quad (12)$$

where  $c_\theta$  represents  $\cos \theta$ ,  $s_\phi$  represents  $\sin \phi$  and so on. Then, the gravitational force denotes  $\mathbf{F}_g = mR^T \mathbf{g}$  where  $m$  is the mass of the robot. As mentioned in Section II, the robot is designed to be neutrally buoyant, with the C. B. and C. M. non-coincident but co-located along an axis parallel to the  $\mathbf{z}$  axis. Hence, the robot buoyancy can be expressed as  $\mathbf{F}_b = -mR^T \mathbf{g}$  in the body-fixed coordinates. We define a vector pointing from the C. M. to C. B. as  $\mathbf{r}_b = [0, 0, h_b]^T$ . Then, the net torque caused by the non-coincident forces [21] is expressed in the body-fixed coordinates as

$$\mathbf{M}_g = \mathbf{r}_b \times \mathbf{F}_b = mR^T \mathbf{g} \times \mathbf{r}_b \quad (13)$$

The robotic fish body also experiences the drag force  $\mathbf{F}_D$  and moment  $\mathbf{M}_b$  [21], [43]. We reasonably assume that the angle of attack of the body is small in steady swimming. As a result, the lift acting on the body is negligible and the drag acting on the robot body takes the form

$$\mathbf{F}_D = -\frac{1}{2} \rho |\mathbf{V}|^2 S C_D \hat{\mathbf{V}} \quad (14)$$

where  $C_D$  is a  $3 \times 3$  matrix and  $S$  is the surface area tensor of the robot body.  $S$  is defined as  $\hat{\mathbf{V}}^T A \hat{\mathbf{V}}$  where  $A = \text{diag}(S_{xx}, S_{yy}, S_{zz})$ .  $S_{xx}$ ,  $S_{yy}$  and  $S_{zz}$  denote respectively the maximum cross-section area of body perpendicular to  $\mathbf{x}$ ,  $\mathbf{y}$  and  $\mathbf{z}$  axes.

Lastly, the drag moment  $\mathbf{M}_b$  was caused by two types of body motion and expressed as  $\mathbf{M}_b = \mathbf{M}_w + \mathbf{M}_v$  where  $\mathbf{M}_w$  is caused by the body rotation while  $\mathbf{M}_v$  is caused by the body velocity. First, it is known that the water can add a damping effect to rotations of the body about its principal axes. This effect [21] is somewhat roughly, but effectively, contained in the model as a simple viscous moment impeding the body's rotation in all directions

$$\mathbf{M}_w = -C_w \boldsymbol{\omega} \quad (15)$$

where  $C_w = \text{diag}(C_{wx}, C_{wy}, C_{wz})$  is a simple damping coefficient. Moreover, the water always strikes on the body while the robot is swimming in the water, which accounts for the waterjet strike force [44], [45] and induces a new torque

$$\begin{cases} M_{vx} = \frac{1}{2} \rho C_{vx} |\mathbf{V}|^2 \left( \frac{V_y}{|V_z|} S_{yy} - \frac{V_z}{|V_y|} S_{zz} \right) \\ M_{vy} = \frac{1}{2} \rho C_{vy} |\mathbf{V}|^2 \left( \frac{V_z}{|V_x|} S_{zz} - \frac{V_x}{|V_z|} S_{xx} \right) \\ M_{vz} = \frac{1}{2} \rho C_{vz} |\mathbf{V}|^2 \left( \frac{V_x}{|V_y|} S_{xx} - \frac{V_y}{|V_x|} S_{yy} \right) \end{cases} \quad (16)$$

where  $C_{vx}$ ,  $C_{vy}$  and  $C_{vz}$  are the moment coefficients for the  $\mathbf{x}$ -axis,  $\mathbf{y}$ -axis and  $\mathbf{z}$ -axis and  $C_v = \text{diag}(C_{vx}, C_{vy}, C_{vz})$  respectively.

### C. Model Formulation

In this study, the robot is modeled as a rigid body with three rigid fins surrounded by an irrotational, inviscid and incompressible fluid. The dynamic equations of the robot are a set of nonlinear, first-order differential equations with respect to the body-fixed frame. Combining Newton's second law for linear motion and Euler's equation for angular motion, these equations are described as follows

$$\begin{bmatrix} \mathbf{F} \\ \mathbf{M} \end{bmatrix} = \begin{bmatrix} \tilde{m}I & 0 \\ 0 & J \end{bmatrix} \begin{bmatrix} \dot{\mathbf{V}} \\ \dot{\boldsymbol{\omega}} \end{bmatrix} + \begin{bmatrix} \boldsymbol{\omega} \times \tilde{m}\mathbf{V} \\ \boldsymbol{\omega} \times J\boldsymbol{\omega} \end{bmatrix} \quad (17)$$

where  $\mathbf{F}$  and  $\mathbf{M}$  are respectively the external force and torque, applied to the center of mass of the robotic fish;  $I \in \mathbb{R}^{3 \times 3}$  is the identity matrix. The cross products represent the Coriolis effect as the body-fixed coordinates are not an inertial frame.  $\tilde{m}$  and  $J$  are respectively the mass and inertia matrices of the robot, including added mass effects. We reasonably assume the robot has three planes of symmetry, then  $\tilde{m} = \text{diag}(m_{xx}, m_{yy}, m_{zz})$ ,  $J = \text{diag}(J_{xx}, J_{yy}, J_{zz})$ . The calculations for  $\tilde{m}$  and  $J$  of robotic fish can be found in [46]. Finally, the 3D model for the robotic fish can be further summarized to the control-affine form

$$\begin{cases} \dot{\mathbf{V}} = \frac{\sum_1^3 (\mathbf{F}_L^i + \mathbf{F}_D^i) + \mathbf{F}_D + \mathbf{F}_g + \mathbf{F}_b - \boldsymbol{\omega} \times \tilde{m}\mathbf{V}}{\tilde{m}} \\ \dot{\boldsymbol{\omega}} = \frac{\sum_1^3 \mathbf{M}_i + \mathbf{M}_w + \mathbf{M}_v - \boldsymbol{\omega} \times J\boldsymbol{\omega}}{J} \end{cases} \quad (18)$$

where all the forces and torques in (18) have been explicitly expressed in above analysis.

Now we can employ numerical methods to simulate the robot model. We use unit quaternions ( $\mathbf{q} = q_0 + q_1\mathbf{i} + q_2\mathbf{j} + q_3\mathbf{k}$ ) to express the robot position and attitude

$$\begin{bmatrix} \dot{X} & \dot{Y} & \dot{Z} \end{bmatrix}^T = C(\mathbf{q})\mathbf{V} \quad (19)$$

$$\phi = \arctan 2(2q_0q_1 + 2q_2q_3, 1 - 2q_1^2 - 2q_2^2) \quad (20)$$

$$\theta = -\arcsin(2q_0q_2 - 2q_1q_3) \quad (21)$$

$$\psi = \arctan 2(2q_0q_3 + 2q_1q_2, 1 - 2q_2^2 - 2q_3^2) \quad (22)$$

where  $C(\mathbf{q})$  is the transformation matrix taking the form

$$C(\mathbf{q}) = \begin{bmatrix} q_0^2 + q_1^2 - q_2^2 - q_3^2 & 2(q_1q_2 - q_0q_3) & 2(q_1q_3 + q_0q_2) \\ 2(q_1q_2 + q_0q_3) & q_0^2 - q_1^2 + q_2^2 - q_3^2 & 2(q_2q_3 - q_0q_1) \\ 2(q_1q_3 - q_0q_2) & 2(q_0q_1 + q_2q_3) & q_0^2 - q_1^2 - q_2^2 + q_3^2 \end{bmatrix} \quad (23)$$

and  $\mathbf{q}$  can be calculated by the following equation

$$\begin{bmatrix} \dot{q}_0 \\ \dot{q}_1 \\ \dot{q}_2 \\ \dot{q}_3 \end{bmatrix} = \frac{1}{2} \begin{bmatrix} 0 & -\omega_x & -\omega_y & -\omega_z \\ \omega_x & 0 & \omega_z & -\omega_y \\ \omega_y & -\omega_z & 0 & \omega_x \\ \omega_z & \omega_y & -\omega_x & 0 \end{bmatrix} \begin{bmatrix} q_0 \\ q_1 \\ q_2 \\ q_3 \end{bmatrix} \quad (24)$$

Synthesizing (18)-(24), we can ultimately solve the kinematic (e.g., robot position, linear velocity, angular velocity and attitudes) and dynamic (e.g., force and moment) parameters through the numerical Runge-Kutta method in a Microsoft Visual Studio environment. As a result, multiple spatial motions of the robotic fish will be broadly generated in simulations and then estimated through extensive experiments below.

### IV. SIMULATION AND EXPERIMENTAL RESULTS

In order to evaluate the effectiveness and the versatility of the developed 3D dynamic model, multimodal swimming behaviors including forward/backward swimming, turning, ascending/descending and rolling and spiraling maneuvers are extensively investigated, both in simulations with the built model and during experiments with the robot.

#### A. Model Parameter Determination

Many coefficients in the model such as the robot mass and moment of inertia can be directly measured or calculated. Some coefficients can be easily measured by simple experiments. For instance, the drag coefficient of the robot body is measured by a force measurement apparatus [47]. However, some coefficients such as the lift and drag coefficients of the flapping fins are difficult to measure. We, therefore, identify them from the experimental motion data.

The unknown hydrodynamic parameters contain the lift coefficients  $c_{L1}^i, c_{L2}^i$  in (5), the drag coefficients  $c_{D0}^i, c_{D1}^i, c_{D2}^i$  in (6), and the moment-related coefficients  $C_{wx}, C_{wy}, C_{wz}, C_{vx}, C_{vy},$  and  $C_{vz}$  in (15) and (16). Preliminary simulations with our model indicate that 1) moment-related parameters do not affect the robot's linear motion and 2) the lift/drag coefficients of the pectoral fins and tail are mutually independent. Further, we assume that the parameters for the left and right pectoral fins are identical considering the identity of the geometrical shapes and the skin material. Therefore, we categorize these unknown parameters into five groups:  $\{c_{L1}^1, c_{L2}^1, c_{D0}^1, c_{D1}^1, c_{D2}^1\}$ ,  $\{c_{L1}^3, c_{L2}^3, c_{D0}^3, c_{D1}^3, c_{D2}^3\}$ ,  $\{C_{wx}, C_{vx}\}$ ,  $\{C_{wy}, C_{vy}\}$  and  $\{C_{wz}, C_{vz}\}$ , which are identified through the motion data respectively from tail-actuated forward swimming, pectoral-fin-propelled forward swimming, pectoral-fin rolling, pectoral-fin pitching, and pectoral-fin turning. The lower and upper bounds are listed in Table II. These bounds are determined by appropriately

TABLE II  
BOUNDS OF THE HYDRODYNAMIC PARAMETERS

Item	$C_{L1}^1$	$C_{L2}^1$	$C_{D0}^1$	$C_{D1}^1$	$C_{D2}^1$	$C_{L1}^3$	$C_{L2}^3$	$C_{D0}^3$
$\lambda_l$	-1	-3	-1	-1	0	-1	-3	-1
$\lambda_u$	1	3	1	1	3	1	3	1
Item	$C_{D1}^3$	$C_{D2}^3$	$C_{wx}$	$C_{wy}$	$C_{wz}$	$C_{vx}$	$C_{vy}$	$C_{vz}$
$\lambda_l$	-1	0	0	0	0	0	0	0
$\lambda_u$	1	3	1	1	1	1	1	1

Note:  $\lambda$  represents the parameters to be identified and the notation  $\lambda_l$  and  $\lambda_u$  denote the lower and upper bounds of  $\lambda$ .

extending the ranges of empirical values from [41], [42].

For each of the above parameter groups, we conduct simulations for all the parameter combinations and extract the simulated linear speed, angular speed, and attitude for each situation. The interval for lift and drag coefficients of the fins is restricted to 0.1 and the interval for moment-related coefficients of the fins is restricted to 0.05. At the same time, we gathered experimental speeds and attitudes when the robot was swimming, in accordance with the specified simulated motion. Finally, we used the least square method to determine the optimal solution for each parameter group. The optimal

solution has the least deviation between the experimental and the simulated motion data. Consequently, we obtain the identified hydrodynamic parameters  $\lambda^*$  listed in Table III. Because of the space limitation, the validation results of these

TABLE III  
PARAMETER VALUES FOR THE MODEL SIMULATION

Item	Value	Item	Value	Item	Value
$m$	3.093 kg	$m_{xx}$	2.517 kg	$m_{yy}$	6.257 kg
$m_{zz}$	6.257 kg	$\rho$	1000 kg/m <sup>3</sup>	$J_{xx}$	0.021 kg·m <sup>2</sup>
$J_{yy}$	0.102 kg·m <sup>2</sup>	$J_{zz}$	0.102 kg·m <sup>2</sup>	$A_{xx}$	0.030 m <sup>2</sup>
$A_{yy}$	0.050 m <sup>2</sup>	$A_{zz}$	0.050 m <sup>2</sup>	$C_D$	0.672
$C_{vx}$	0.025 m <sup>3</sup>	$C_{vy}$	0.050 m <sup>3</sup>	$C_{vz}$	0.050 m <sup>3</sup>
$C_{wx}$	0.015 m/s	$C_{wy}$	0.010 m <sup>3</sup>	$C_{wz}$	0.020 m/s
$C_{L1}^1$	0.500	$C_{L2}^1$	-0.200	$C_{D0}^1$	0.100
$C_{D1}^1$	0.000	$C_{L2}^2$	2.500	$C_{L1}^2$	0.500
$C_{L2}^2$	-0.200	$C_{D0}^2$	0.100	$C_{D1}^2$	0.000
$C_{D2}^2$	2.500	$C_{L1}^3$	0.800	$C_{L2}^3$	-0.200
$C_{D0}^3$	0.100	$C_{D1}^3$	0.000	$C_{D2}^3$	2.500
$S_1$	0.00875 m <sup>2</sup>	$S_2$	0.00560 m <sup>2</sup>	$S_3$	0.00560 m <sup>2</sup>
$a_l$	0.06 m	$b_l$	0.050 m	$c_l$	0.000 m
$a_r$	0.060 m	$b_r$	0.050 m	$c_r$	0.000 m
$a_t$	0.100 m	$b_t$	0.000 m	$c_t$	0.000 m
$r_x$	0.030 m	$r_y$	0.050 m	$r_z$	0.140 m
$h_b$	-0.005 m				

coefficients are not presented here. However, the following systematic comparisons between simulations and experiments soundly validate the effectiveness of these coefficients in the 3D dynamic model.

### B. Experimental Description

Multimodal swimming behaviors were conducted both in simulations and experiments in which the robot motion data such as the robot position, linear and angular velocities, and attitude were recorded. The planar motions (forward/backward swimming and turning) experiments were performed in a 300 cm × 200 cm × 20 cm tank and the 3D motions (pitching, rolling and spiraling) experiments were performed in a 400 cm × 200 cm × 90 cm tank. Both the simulations and experiments are performed in an open loop. Planar position and velocity of the robot in the experiments are obtained through our online vision tracking system [48], as shown in Fig. 5(a). The online tracking system contains an overhead camera, a robust tracking algorithm providing real-time tracking of moving robots on a water surface, and a computer to receive the video stream and run the tracking algorithm [48]. A Kalman filter was applied to smooth the tracking results to remove the noise during tracking. Note that the motion tracking platform is not integrated into the robot, and it is an independent system for the identification of the robot motion. Robot attitude and angular velocity are collected from an onboard IMU whose sampling rate is 50 Hz. The accuracy for yaw, pitch, roll, and angular velocity are respectively 2°, 1° and 1°, and 0.5°/s. Moreover, the vertical position and velocity of the robot is measured by the onboard pressure sensor, according to the following formula

$$p = \rho gh \quad (25)$$

where  $p$  is the pressure,  $h$  is the depth of water and  $\rho$  is the density of the water. Snapshots of the typical swimming

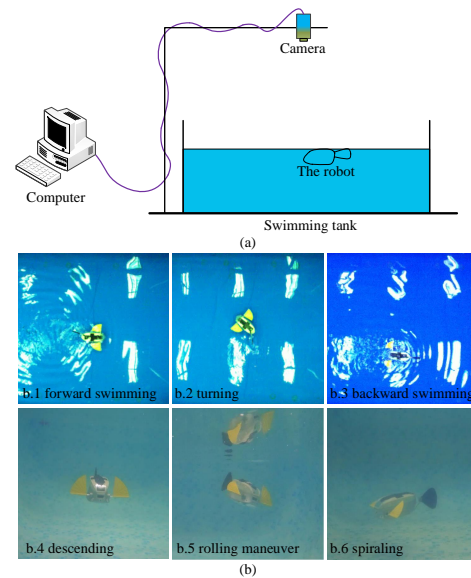


Fig. 5. Experimental platform and typical motions in the experiments. (a) Experimental setup and (b) the explored typical motions.

behaviors explored by the developed 3D model are illustrated in Fig. 5(b).

### C. Rectilinear Motion

The first experiment focused on the model performance of rectilinear motion including forward and backward swimming. We first present a forward swimming case to compare the simulated and experimental data in Fig. 6. The characteristic

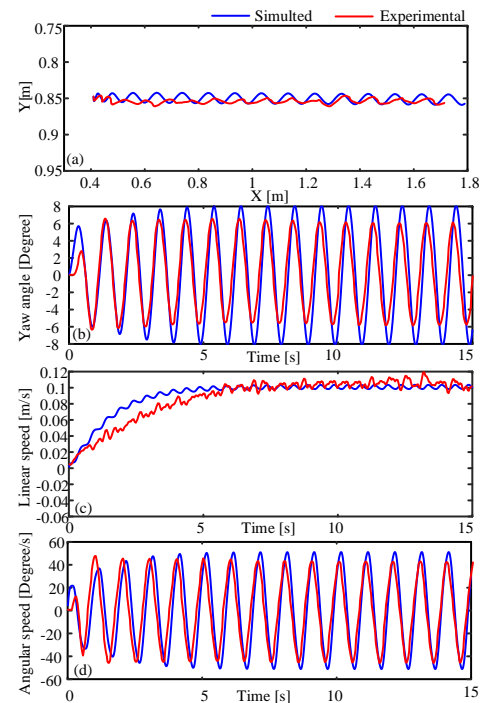


Fig. 6. Comparative tests of forward swimming at  $f = 1.0$  Hz, which contain the trajectories (a), yaw angles (b) and linear (c) and angular speeds (d). Note that displacements  $X$ ,  $Y$  and yaw angle are in the global inertial reference frame. Linear and angular velocities are in the body-fixed frame.

parameters of the adopted CPGs were set as:  $f = 1.0$  Hz,  $P_1 = P_2 = 0$ ,  $P_3 = 15^\circ$ ,  $O_1 = O_2 = O_3 = 0$ . As can be seen, experimental trajectories, yaw angle, linear and angular velocities are in good agreement with simulated data, verifying the effectiveness of the built dynamic model. More specifically, from Fig. 6(a), (b), and (d), it can be seen that the simulated data also basically capture the axial and lateral oscillations in fish swimming which have been nicely demonstrated by biologists [49]. Similarly, previous robotic fish models [20]–[22], [26] also exhibited these oscillatory features while swimming. Therefore, although the oscillation in linear speed (Fig. 6(c)) cannot be directly compared because of the limited accuracy of our current localization system, we can reasonably deduce that the real linear speed of the robot will also oscillate periodically, similar to the simulated linear speed.

Moreover, rectilinear motions are compared systematically within the available CPG parameter space to validate the versatility of the established dynamic model. Although forward motion can be selectively achieved by the tail, by the pectoral fins, or by a combination of the tail and the pectoral fins, we choose tail-driven forward mode as a representation of forward motion. On the other hand, the backward motion is implemented by flapping the pectoral fins with zero offsets. For both forward and backward motions, the explored frequency was changed every 0.1 Hz from 0.5 Hz to 1.5 Hz, and the amplitude was changed every  $5^\circ$  from  $10^\circ$  to  $30^\circ$ . Each experiment was performed 5 times to reduce errors.

Fig. 7(a) and (b) show the comparison between the simulated and experimental forward speeds; Fig. 7(c) and (d) show the comparison between the simulated and experimental backward speeds. It can be seen that the simulated data are in fairly acceptable agreement with the experimental data. More specifically, the average prediction error of the developed model for forward and backward motions are respectively 14.30% and 20.88% among the whole CPG parameter space. Both the simulated and experimental rectilinear velocities increase with beating frequency and with amplitude. More careful inspection indicates that both the simulated forward and backward speeds exhibit relatively larger discrepancies with experimental data at higher actuation frequency and amplitude. This unconformity is probably caused by the limited torques of the adopted servomotors of the robot. Furthermore, it is interesting to note that the backward velocities here are comparable to the tail-actuated forward speed, suggesting that the pectoral fins can not only improve robot maneuverability and balance but also contribute a lot to robot propulsion.

#### D. Turning Motion

In this subsection, we estimate the model versatility for turn maneuvers within a wide range of parameter space. Similar to forward motion, turning maneuvers can be implemented by several different fin combinations. Here the offset of the flapping tail is used to accomplish a turning maneuver. Moreover, we restrict the tail amplitude to  $15^\circ$  both in simulations and experiments. The beating frequency was changed every 0.1 Hz from 0.5 Hz to 1.5 Hz, and the tail offset was changed every  $5^\circ$  from  $15^\circ$  to  $40^\circ$ . Each experiment was performed 5

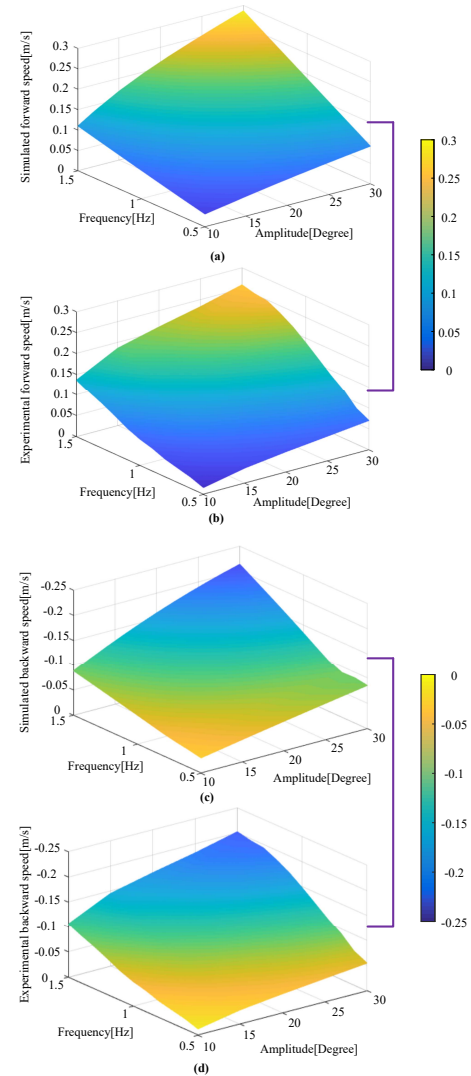


Fig. 7. Comparisons of simulated and experimental rectilinear (forward and backward) speed for different frequencies and amplitudes.

times to reduce errors. Fig. 8 (a) and (c) show the simulated turning speed and radius respectively, and Fig. 8 (b) and (d) depict the experimental turning speed and radius respectively. It is clear that the turning speed increases with the beating frequency and oscillation offset, and that the turning radius decreases with the oscillation offset. Interestingly, however the turning radius is constant with the beating frequency. Although there are some discrepancies in the high speed area, the built model basically predicts the robot’s turning speed and turning radius within a large-scale parameter space, validating the versatility of developed dynamic model for turning motions on the whole. The average errors of the dynamic model in the prediction of turning speed and radius are respectively 19.2% and 8.9% within the explored parameter space. Similarly, the visible discrepancies between the simulation and experimental results at high actuation frequency and large amplitude are largely caused by the limitation of servo motor torque. As can be observed, the turning speed increases with the beating frequency and oscillation offset. Moreover, the turning radius also increases with the oscillation offset. However, it

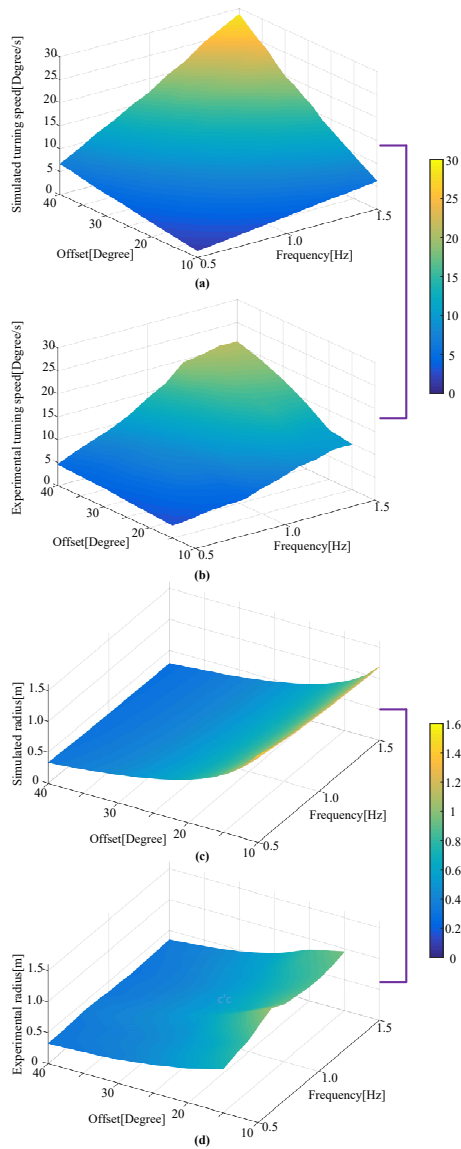


Fig. 8. Comparisons of simulated (a) and experimental (b) turning speed, and of simulated (c) and experimental (d) turning radius for different beating frequencies and offsets.

is interesting that the turning radius is approximately constant with the beating frequency. These intrinsic relations will greatly facilitate motion controller design and path planning for robotic fish in real applications that require various turning conditions.

### E. Pitching Motion

Next, we explored the performance of the dynamic model in predicting pitching motions. Fig. 9 shows the comparison between the simulated and experimental data where the robot started to ascend from rest where the CPG parameters are  $f = 1.5$  Hz,  $P_1 = P_2 = 15^\circ$ ,  $P_3 = 0$ ,  $O_1 = O_2 = -45^\circ$ ,  $O_3 = 0$ . As can be seen, experimental results are in good agreement with simulated data, verifying the effectiveness of the established dynamic model. More specifically, the negative speed in the vertical direction in Fig. 9(a) indicates the robot is

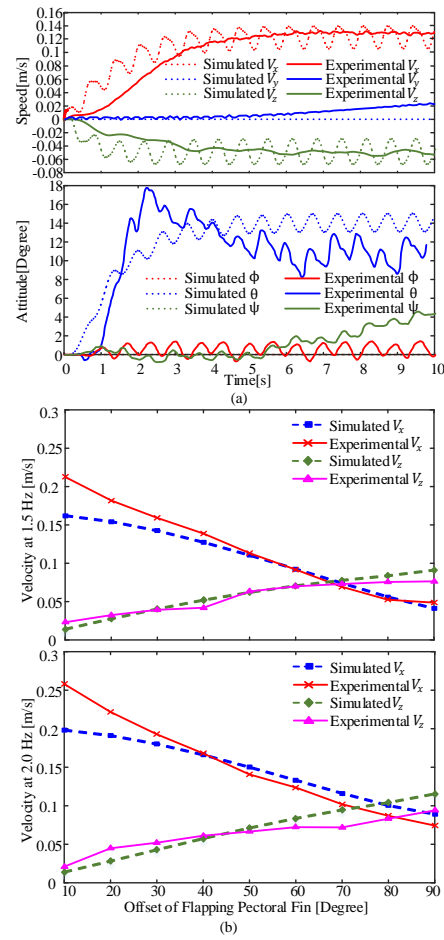


Fig. 9. Comparison of simulated and experimental data for pitching maneuver. (a) Speeds and attitudes for a certain ascending behavior; (b) velocities for different offsets of pectoral fins at two fixed frequencies.

swimming upwards. The simulated forward velocity (0.122 m/s) and vertical velocity ( $-0.051$  m/s) during steady state are close to the experimental velocities (0.133 m/s,  $-0.045$  m/s) of the robot. Moreover, the positive pitch angle in Fig. 9(a) also indicates that the robot is raising its head while ascending. It is evident that the model basically predicts the robot's velocities and attitudes for pitching motion.

Moreover, to validate the versatility of the built model for pitching maneuvers, we compared the simulations and the experimental results in descending motions. The amplitude of the pectoral fins is fixed at  $15^\circ$  while the tail keeps straight and stationary in the experiment. Two fixed beating frequencies, 1.5 Hz and 2.0 Hz, are investigated, and the oscillation offset of the pectoral fins is changed every  $10^\circ$  from  $10^\circ$  to  $90^\circ$  in the experiment. Descending behavior was performed 5 times for each combination of the CPG parameters. Fig. 9(b) compares the simulated and experimental data for horizontal velocities  $V_x$  and vertical velocities  $V_z$  of the robot. As mentioned earlier,  $V_x$  is recorded by an overhead camera and  $V_y$  is evaluated by the robot's onboard pressure sensors. As can be observed, the built model basically predicted the robot's horizontal and vertical velocities among a wide range of CPG parameter space. The error of the dynamic model for horizontal speed prediction and

vertical speed are respectively 11.6% and 8.7%. Considering the model simplification and the parameter mismatch to a certain extent, the results are quite reasonable. Additionally, it is clear that  $V_x$  decreases with the pectoral fin offset while  $V_y$  increases with the fin offset. These patterns will greatly facilitate the robot's pitching control in the future.

### F. Rolling Maneuver

Rolling maneuver which is largely ignored in fish robot modeling was studied here for our dynamic model. As we mentioned earlier, the C. M. of the robot is below the C. B.. As a result, it is hard to achieve continuous rotation about the longitudinal axis of the robot body. Nevertheless, small scale rolling maneuvers can still be observed through the coordination of the pectoral fins. More specifically, the rolling maneuver was achieved by the asymmetrical amplitude of the pectoral fins with a nonzero oscillation offset. Note that the asymmetrical amplitude actuation of the pectoral fins produces not merely rolling motion, but also pitching and yawing maneuvers. To be specific, the torque along the y-axis of the body are formed because of the offset of the pectoral fins, thereby tilting the robot in pitching. Moreover, the asymmetrical amplitude of the pectoral fins will form torques along the x-axis and z-axis of the body, hence generating rolling and yawing respectively. The comparison between the simulated and the experimental data for rolling maneuver are illustrated in Fig. 10. The specific CPG parameters are

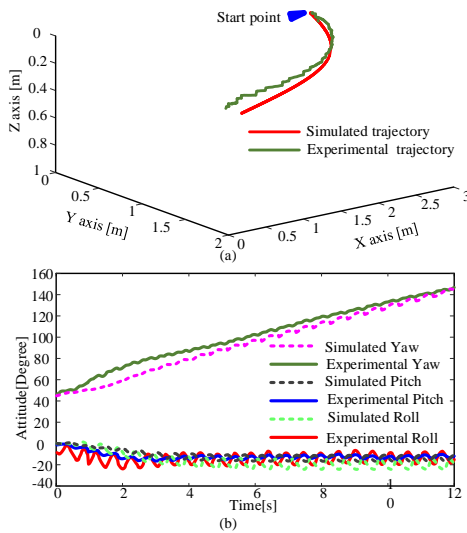


Fig. 10. Comparisons of simulated and experimental results for rolling maneuver. (a) Robot trajectory and (b) robot attitude.

$f = 1.9$  Hz,  $P_1 = 25^\circ$ ,  $P_2 = 10^\circ$ ,  $P_3 = 0$ ,  $O_1 = O_2 = 30^\circ$ , and  $O_3 = 0$ . As a whole, the model predicts the robot's 3D trajectory nicely, and it also predicts the robot's yaw, pitch, and roll angles satisfactorily, verifying the effectiveness of the developed dynamic model in predicting complicated motions such as the rolling maneuver.

### G. Spiral Motion

3D spiral motion represents one of the highest forms of maneuverability for robotic fish. Finally, 3D spiral motion

was explored with the developed model and experimentally validated, as shown in Fig. 11. The motion is achieved by

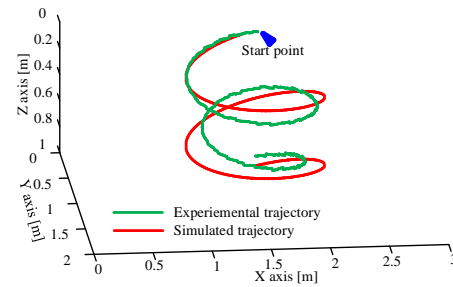


Fig. 11. Simulated and experimental spiral motion in 3D environment (side view).

the ascending/descending motion combined with a deflected tail. A deflected tail means the robot tail has a nonzero offset  $O_3$  which produces rotating torque while moving. The adopted CPG parameters for the model and the experiment are  $f = 1.1$  Hz,  $P_1 = P_2 = 10^\circ$ ,  $P_3 = 0$ ,  $O_1 = O_2 = 8^\circ$ ,  $O_3 = 35^\circ$ . In the experiment, the robot starts spiraling down from the water surface and approaches the bottom of the pool after 60 seconds. As can be seen, the experimental trajectory is basically in agreement with the simulated trajectory. The average position error between the simulation and experiments are 24.8% during the spiral motion. Although there is a visible difference between the simulated and experimental trajectory, the results are fairly acceptable considering the model simplification. The success of spiral motion predictions indicates that the proposed 3D dynamic model is suitable and promising for future motion control and planning studies in 3D space. To the best of our knowledge, this is the first dynamic model prediction and experimental verification of the 3D spiral motion for robotic fish.

## V. CONCLUSION AND FUTURE WORK

In this study, we have developed a complete 3D dynamic model for robotic fish actuated by a pair of independent pectoral fins and a caudal fin. The model considers the simplified lift and drag acting on the fins and the robot body, the gravity and the buoyancy, and the waterjet strike force. The critical lift and drag of flapping fins are derived with an explicit 3D angle of attack for the first time, which contributes a lot to the success of complex 3D motions. Combining Newton's second law for linear motion and Euler's equation for angular motion, the 3D dynamics equations of the robot are formulated.

Simulations show that the model is able to predict multimodal swimming behaviors of the robot, such as forward and backward swimming, turning, pitch maneuvers, and even complicated motions such as rolling and spiraling. Comparisons between the simulated and experimental trajectory, velocity, and attitude of the robot have demonstrated the effectiveness of the 3D dynamic model in describing multiple swimming modes. Furthermore, we systematically compared the simulated and experimental data over an extensive range of CPG control parameter space for forward, backward, turning and pitching motions. These results verify that the dynamic

model can always predict the robot's velocities and attitudes satisfactorily within large scopes of control parameters, strongly validating the versatility of the dynamic model for the fin-actuated robotic fish. In summary, the work presented in this paper provides a versatile 3D dynamic model capable of predicting multiple 3D motions for the pectoral and caudal fin actuated robotic fish. The developed 3D dynamic model is formulated in a control-affine form and therefore will facilitate the design of 3D motion controllers for robotic fish.

This work can be extended in several directions. We will first explore the analytical insights of the model to facilitate further controller design for the robot. Moreover, based on the proposed 3D dynamic model, we will design model-based path planning controllers such as a model predictive controller for the robotic fish.

## REFERENCES

- [1] R. Du, Z. Li, K. Youcef-Toumi, and P. Valdivia y Alvarado, "Robot fish," *Berlin, Heidelberg: Springer*, vol. 10, pp. 978–3, 2015.
- [2] P. R. Bandyopadhyay, "Maneuvering hydrodynamics of fish and small underwater vehicles," *Integrative and Comparative Biology*, vol. 42, no. 1, pp. 102–117, 2002.
- [3] J. Liu, H. Hu, and D. Gu, "A hybrid control architecture for autonomous robotic fish," in *2006 IEEE/RSJ International Conference on Intelligent Robots and Systems*. IEEE, 2006, pp. 312–317.
- [4] J. D. Liu and H. Hu, "Biologically inspired behaviour design for autonomous robotic fish," *International Journal of Automation and Computing*, vol. 3, no. 4, pp. 336–347, 2006.
- [5] J. Yu, R. Ding, Q. Yang, M. Tan, W. Wang, and J. Zhang, "On a bio-inspired amphibious robot capable of multimodal motion," *IEEE/ASME Transactions on Mechatronics*, vol. 17, no. 5, pp. 847–856, 2012.
- [6] P. Kodati, J. Hinkle, A. Winn, and X. Deng, "Microautonomous robotic ostraciiform (marco): Hydrodynamics, design, and fabrication," *IEEE Transactions on Robotics*, vol. 24, no. 1, pp. 105–117, 2008.
- [7] W. Wang and G. Xie, "Online high-precision probabilistic localization of robotic fish using visual and inertial cues," *IEEE Transactions on Industrial Electronics*, vol. 62, no. 2, pp. 1113–1124, 2015.
- [8] W. Wang, D. Gu, and G. Xie, "Autonomous optimization of swimming gait in a fish robot with multiple onboard sensors," *IEEE Transactions on Systems, Man, and Cybernetics: Systems*, vol. PP, no. 99, pp. 1–13, 2017.
- [9] C. Zhou and K. H. Low, "Design and locomotion control of a biomimetic underwater vehicle with fin propulsion," *IEEE/ASME Transactions on Mechatronics*, vol. 17, no. 1, pp. 25–35, 2012.
- [10] L. Wen, T. M. Wang, G. H. W, and J. H. Liang, "Quantitative thrust efficiency of a self-propulsive robotic fish: Experimental method and hydrodynamic investigation," *IEEE/ASME Transactions on Mechatronics*, vol. 18, no. 3, pp. 1027–1038, 2013.
- [11] S. Zhang, Y. Qian, P. Liao, F. Qin, and J. Yang, "Design and control of an agile robotic fish with integrative biomimetic mechanisms," *IEEE/ASME Transactions on Mechatronics*, vol. 21, no. 4, pp. 1846–1857, 2016.
- [12] Y. Zhong, Z. Li, and R. Du, "A novel robot fish with wire-driven active body and compliant tail," *IEEE/ASME Transactions on Mechatronics*, vol. 22, no. 4, pp. 1633–1643, 2017.
- [13] A. D. Marchese, C. D. Onal, and D. Rus, "Autonomous soft robotic fish capable of escape maneuvers using fluidic elastomer actuators," *Soft Robotics*, vol. 1, no. 1, pp. 75–87, 2014.
- [14] F. Zhang, O. En-Nasr, E. Litchman, and X. Tan, "Autonomous sampling of water columns using gliding robotic fish: Control algorithms and field experiments," in *2015 IEEE International Conference on Robotics and Automation (ICRA)*, 2015, pp. 517–522.
- [15] Y.-S. Ryuh, G.-H. Yang, J. Liu, and H. Hu, "A school of robotic fish for mariculture monitoring in the sea coast," *Journal of Bionic Engineering*, vol. 12, no. 1, pp. 37–46, 2015.
- [16] Z. Wu, J. Liu, J. Yu, and H. Fang, "Development of a novel robotic dolphin and its application to water quality monitoring," *IEEE/ASME Transactions on Mechatronics*, vol. pp, no. 99, pp. 1–11, 2017.
- [17] D. Zhang, L. Wang, J. Yu, and M. Tan, "Coordinated transport by multiple biomimetic robotic fish in underwater environment," *IEEE Transactions on Control Systems Technology*, vol. 15, no. 4, pp. 658–671, 2007.
- [18] Y. Jia and L. Wang, "Leader-follower flocking of multiple robotic fish," *IEEE/ASME Transactions on Mechatronics*, vol. 30, no. 3, pp. 1–12, 2015.
- [19] S. D. Kelly and R. M. Murray, "Modelling efficient pisciform swimming for control," *International Journal of Robust and Nonlinear Control*, vol. 10, no. 4, pp. 217–241, 2000.
- [20] F. Boyer, M. Porez, and W. Khalil, "Macro-continuous computed torque algorithm for a three-dimensional eel-like robot," *IEEE Transactions on Robotics*, vol. 22, no. 4, pp. 763–775, 2006.
- [21] K. A. Morgansen, B. I. Triplett, and D. J. Klein, "Geometric methods for modeling and control of free-swimming fin-actuated underwater vehicles," *IEEE Transactions on Robotics*, vol. 23, no. 6, pp. 1184–1199, 2007.
- [22] J. Wang and X. Tan, "Averaging tail-actuated robotic fish dynamics through force and moment scaling," *IEEE Transactions on Robotics*, vol. 31, no. 4, pp. 906–917, 2015.
- [23] J. Yu, J. Yuan, Z. Wu, and M. Tan, "Data-driven dynamic modeling for a swimming robotic fish," *IEEE Transactions on Industrial Electronics*, vol. 63, no. 9, pp. 5632–5640, 2016.
- [24] M. Lighthill, "Note on the swimming of slender fish," *J. Fluid Mech*, vol. 9, no. 2, pp. 305–317, 1960.
- [25] M. J. Lighthill, "Large-amplitude elongated-body theory of fish locomotion," *Proceedings of the Royal Society B: Biological Sciences*, vol. 179, no. 1055, pp. 125–138, 1971.
- [26] J. Yu, M. Wang, Z. Su, M. Tan, and J. Zhang, "Dynamic modeling of a CPG-governed multijoint robotic fish," *Advanced Robotics*, vol. 27, no. 4, pp. 275–285, 2013.
- [27] L. Li, C. Wang, and G. Xie, "Modeling of a carangiform-like robotic fish for both forward and backward swimming: Based on the fixed point," in *2014 IEEE International Conference on Robotics and Automation (ICRA)*, 2014, pp. 800–805.
- [28] H. E. Daou, T. Salumae, L. D. Chambers, W. M. Megill, and M. Kruusmaa, "Modelling of a biologically inspired robotic fish driven by compliant parts," *Bioinspiration & Biomimetics*, vol. 9, no. 1, p. 016010, 2014.
- [29] L. Li, C. Wang, R. Fan, and G. Xie, "Exploring the backward swimming ability of a robotic fish: Combining modelling and experiments," *International Journal of Advanced Robotic Systems*, vol. 13, no. 5, pp. 1–10, 2016.
- [30] E. Kanso, J. E. Marsden, C. W. Rowley, and J. B. Melli-Huber, "Locomotion of articulated bodies in a perfect fluid," *Journal of Nonlinear Science*, vol. 15, no. 4, pp. 255–289, 2005.
- [31] Y. Hu, W. Zhao, and L. Wang, "Vision-based target tracking and collision avoidance for two autonomous robotic fish," *IEEE Transactions on Industrial Electronics*, vol. 56, no. 5, pp. 1401–1410, 2009.
- [32] W. Wang and G. Xie, "Dynamic modeling of an ostraciiform robotic fish based on angle of attack theory," in *2014 IEEE World Congress on Computational Intelligence (WCCI)*, 2014, pp. 3944–3949.
- [33] J. Carling, T. L. Williams, and G. Bowtell, "Self-propelled anguilliform swimming: Simultaneous solution of the two-dimensional navier-stokes equations and newton's laws of motion," *Journal of Experimental Biology*, vol. 201, no. 23, pp. 3143–3166, 1998.
- [34] G. V. Lauder, P. G. Madden, R. Mittal, H. Dong, and M. Bozkurtas, "Locomotion with flexible propulsors: I. experimental analysis of pectoral fin swimming in sunfish," *Bioinspiration & Biomimetics*, vol. 1, no. 4, p. S25, 2006.
- [35] P. Alvarado and K. Youcef-Toumi, "Design of machines with compliant bodies for biomimetic locomotion in liquid environments," *Journal of Dynamic Systems Measurement and Control*, vol. 128, no. 1, pp. 3–13, 2006.
- [36] V. Kopman and M. Porfiri, "Design, modeling, and characterization of a miniature robotic fish for research and education in biomimetics and bioinspiration," *IEEE/ASME Transactions on Mechatronics*, vol. 18, no. 2, pp. 471–483, 2013.
- [37] J. Wang and X. Tan, "A dynamic model for tail-actuated robotic fish with drag coefficient adaptation," *Mechatronics*, vol. 23, no. 6, pp. 659–668, 2013.
- [38] W. Wang, J. Guo, Z. Wang, and G. Xie, "Neural controller for swimming modes and gait transition on an ostraciiform fish robot," in *IEEE/ASME International Conference on Advanced Intelligent Mechatronics (AIM)*, 2013, pp. 1564–1569.
- [39] W. Wang and G. Xie, "CPG-based locomotion controller design for a boxfish-like robot," *International Journal of Advanced Robotic Systems*, vol. 11, no. 87, pp. 1–11, 2014.
- [40] L. Li, C. Wang, and G. Xie, "A general CPG network and its implementation on the microcontroller," *Neurocomputing*, vol. 167, pp. 299–305, 2015.

[41] A. J. Healey, S. M. Rock, S. Cody, D. Miles, and J. P. Brown, "Toward an improved understanding of thruster dynamics for underwater vehicles," *IEEE Journal of Oceanic Engineering*, vol. 20, no. 4, pp. 354–361, 1995.

[42] L. N. Cooper, N. Sedano, S. Johansson, B. May, J. D. Brown, C. M. Holliday, B. W. Kot, and F. E. Fish, "Hydrodynamic performance of the minke whale (*balaenoptera acutorostrata*) flipper," *Journal of Experimental Biology*, vol. 211, no. 12, pp. 1859–1867, 2008.

[43] R. Mason and J. W. Burdick, "Experiments in carangiform robotic fish locomotion," in *IEEE International Conference on Robotics and Automation (IRCA)*, 2000, pp. 428–435.

[44] W. Wu, *Fluid Dynamics (Volume one)*, 1st ed. Beijing, China: Peking University Press, 2006.

[45] R. J. Garde, *Fluid Mechanics through problems*. New Age International, 1997.

[46] T. I. Fossen, *Guidance and control of ocean vehicles*. West Sussex PO19 1UD, England: John Wiley & Sons Ltd, 1994.

[47] A. Liu, J. Zhao, L. Li, and G. Xie, "Micro-force measuring apparatus for robotic fish: Design, implementation and application," in *27th Chinese Control and Decision Conference (CCDC)*, 2015, pp. 4938–4943.

[48] L. Shao and G. Xie, "Real-time tracking of moving objects on a water surface," in *IEEE International Conference on Mechatronics and Automation (ICMA)*, 2012, pp. 2114–2119.

[49] E. Tytell, "Do trout swim better than eels? challenges for estimating performance based on the wake of self-propelled bodies," in *Animal Locomotion*, G. Taylor, M. Triantafyllou, and C. Tropea, Eds. Springer Berlin Heidelberg, 2010, pp. 63–74.



**Banti H. Gheneti** was born in Amsterdam, the Netherlands in 1995. He received a B.S. in Computer Science and Electrical Engineering at the Massachusetts Institute of Technology, Cambridge in 2017 and is currently pursuing an M.Eng. there in Electrical Engineering and Computer Science with a concentration in Artificial Intelligence. In 2017 he was a Lab Assistant for the Robotics Science and Systems class at the Massachusetts Institute of Technology. He is a Research Assistant with the Senseable City Laboratory where he coordinates software design and researches perception for autonomous boats. His research interests include 3D object detection and classification, and trajectory prediction.



**Yang Ding** was born in Xinjiang, China in 1982. He received the B.S. in Physics from the University of Science and Technology of China, Hefei, Anhui, China in 2005 and the Ph.D. degree in Physics from Georgia Institute of Technology, Atlanta, Georgia, USA in 2011. He was a Postdoc Fellow at Georgia Institute of Technology from 2011 to 2012 and at University of Southern California from 2012 to 2014. In 2014, he became a Research Assistant Professor at Beijing Computational Science Research Center in Beijing, China, and was promoted as an Assistant Professor in 2015. He is the author of 19 papers. His research interests include bioinspired robots, animal locomotion, complex interaction between organisms and environments, and biofluids. Dr. Ding was a recipient of Robotics: Science & Systems Best paper award in 2010 and was selected into the Recruitment Program of Global Young Experts in 2015.



**Wei Wang** received the B.E. in Automation from University of Electronic Science and Technology of China, Chengdu, Sichuan, China and the Ph.D. degree in General Mechanics and Foundation of Mechanics from Peking University, Beijing, China in 2010 and 2016, respectively. He is now a Post-doctoral Researcher in the Department of Urban Studies and Planning at Massachusetts Institute of Technology. His current research interests include bioinspired robots, underwater robots, driverless vehicle, dynamics and control, and swarm robotics.

Professor in 2015. He is the author of 19 papers. His research interests include bioinspired robots, animal locomotion, complex interaction between organisms and environments, and biofluids. Dr. Ding was a recipient of Robotics: Science & Systems Best paper award in 2010 and was selected into the Recruitment Program of Global Young Experts in 2015.



**Xia Dai** received the B.E. in Electronic Information Engineering from University of Electronic Science and Technology of China, Chengdu, Sichuan, China and the M.Eng. degree in Transportation Information Engineering and Control from Beihang University, Beijing, China, in 2010 and 2013, respectively. During her graduate school, her research interests focused on information network economics, with particular interests on game theory, congestion networks, network coding, and resource allocation optimization. Her current research interests include big data analytics, machine learning and data science.



**Junzhi Yu** (SM'14) received the B.E. degree in safety engineering and the M.E. degree in precision instruments and mechatronics from the North University of China, Taiyuan, China, in 1998 and 2001, respectively, and the Ph.D. degree in control theory and control engineering from the Institute of Automation, Chinese Academy of Sciences (IACAS), Beijing, China, in 2003.

He is currently a Professor with the State Key Laboratory of Management and Control for Complex Systems, IACAS. His research interests include biomimetic robots, intelligent control, and intelligent mechatronic systems.

Dr. Yu serves as the Associate Editors of *IEEE Transactions on Robotics* and *IEEE/ASME Transactions on Mechatronics*.



**Liang Li** received the B. E. degree in automation from Chongqing University, Chongqing, China, and the Ph. D. degree in General Mechanics and Foundation of Mechanics from Peking University, Beijing China, in 2011 and 2017, respectively. He is currently a Post-Doctoral Research Fellow in the Department of Collective Behaviour, Max-Planck Institute for Ornithology, Konstanz, Germany. His current research interests include bio-inspired robots, collective behaviour in hybrid animal-robot systems, biofluid dynamics in fish school and swarm intelligence in robots.



**Guangming Xie** received his B.S. degrees in both Applied Mathematics and Electronic and Computer Technology, his M.E. degree in Control Theory and Control Engineering, and his Ph.D. degree in Control Theory and Control Engineering from Tsinghua University, Beijing, China in 1996, 1998, and 2001, respectively. Then he worked as a postdoctoral research fellow in the Center for Systems and Control, Department of Mechanics and Engineering Science, Peking University, Beijing, China from July 2001 to June 2003. In July 2003, he joined the Center as a lecturer. Now he is a Full Professor of Dynamics and Control in the College of Engineering, Peking University. He is an Associate Editor of Scientific Reports, International Journal of Advanced Robotic Systems, Mathematical Problems in Engineering and an Editorial Board Member of the Journal of Information and Systems Science. His research interests include smart swarm theory, multi-agent systems, multi-robot cooperation, biomimetic robot, switched and hybrid systems, and networked control systems.